PHYSICAL REVIEW B **109**, 094302 (2024)

Evidence for reentrant quantum paraelectric state preceded by a multiglass phase with a nonclassical exponent and magnetodielectric coupling in $SrFe_{12}O_{19}$

Keshav Kumar[1,2] and Dhananjai Pandey[1,3,4]

[1]*School of Materials Science and Technology, Indian Institute of Technology (Banaras Hindu University), Varanasi 221005, India*
[2]*New Chemistry Unit, International Centre for Materials Science, Jawaharlal Nehru Centre for Advanced Scientific Research, Jakkur, Bengaluru 560064, India*
[3]*Department of Materials Science and Metallurgical Engineering, Indian Institute of Technology Bhilai, Raipur 492015, India*
[4]*Department of Physics, Banaras Hindu University, Varanasi 221005, India*

(Received 27 May 2023; revised 27 January 2024; accepted 29 January 2024; published 6 March 2024)

Evidence is presented for a reentrant quantum paraelectric (QPE) state preceded by a dipole glass (DG) phase with a nonclassical exponent in the quantum critical regime of $SrFe_{12}O_{19}$. It is shown that the DG transition is accompanied by a spin glass (SG) transition. Further, the ergodic symmetry-breaking temperatures for the DG and SG transitions coincide ($T_{DG} \sim T_{SG}$) within ±1 K suggesting that $SrFe_{12}O_{19}$ exhibits a canonical multiglass state. It is shown that these transitions are coupled through biquadratic and lower order couplings of two diverse order parameter fields. The stability of the dipole glass state is enhanced magnetically as evidenced by the increase in the freezing temperature with magnetic field (H). The reentrant QPE state, on the other hand, is found to give way to another frequency-dependent peak in the temperature dependence of dielectric constant, most likely a DG phase, under dc magnetic field (H). Further, this transition is not linked to any magnetic transition, in sharp contrast to the higher temperature multiglass transition. The transition temperature of this phase decreases with increasing magnetic field for a fixed frequency unlike the higher temperature DG transition. This raises the possibility of locating a quantum critical point (QCP) in this system at a higher magnetic field than that used in the present work. These results are discussed in the light of quantum critical models of multiferroic transitions. Our results highlight the need for more theoretical studies specific to multiferroic quantum criticality in multiglass systems.

DOI: 10.1103/PhysRevB.109.094302

I. INTRODUCTION

Quantum phase transitions (QPTs) continue to evince considerable interest [1–3] going well beyond its traditional domains of applications to metallic ferromagnetism, heavy fermions, geometrically frustrated two-dimensional antiferromagnets, topological systems, and superconductors to other systems such as ferroelectrics [4], confined water molecules [5], and quantum computing [6,7]. QPTs occur at the experimentally inaccessible zero temperature (0 K) as a result of variation of a nonthermal control parameter (g), such as pressure, composition, and electric and magnetic fields, which destabilizes the quantum disordered or symmetric state, by suppressing the quantum fluctuations, and stabilizes a quantum ordered state with broken symmetry [1]. However, the real interest in the QPT systems lies in the experimentally accessible quantum critical regime (QCR), above the QCP, where both the quantum ($\hbar\omega_0$) and thermal ($k_B T$) fluctuations compete and give rise to various exotic quantum states of matter with a potential for technological applications and new physics [1,2]. Unlike the classical systems, the potential and kinetic energy parts of the Hamiltonian do not commute in the quantum systems but may be mapped to a classical system in ($d + z$) dimension, where z is the dynamical exponent for the dispersion relationship [1]. QPTs have already been shown to have a profound impact on several high-temperature phenomena such as superconductivity in cuprates [8] and Mott insulators [9].

The studies on the marginal/incipient ferroelectrics (FEs) of displacive type, such as $SrTiO_3$ and $KTaO_3$, which are prevented from entering into a long-range ordered FE state even at low temperatures (down to millikelvin) due to quantum fluctuations [10–13] have witnessed a spurt in recent times due to their potential for technological applications (e.g., see [14–17]) and the emergence of new physics (e.g., see [18–22]). The dielectric constant ε_r of both $SrTiO_3$ and $KTaO_3$ [10–13] increases with decreasing temperature as per Curie-Weiss (C-W) law while the square of the TO mode frequency (ω_{TO}^2) decreases linearly with temperature [23–26], consistent with the Lyddane-Sachs-Teller relationship [26], up to a characteristic temperature T_1. Below T_1, the $\varepsilon_r(T)$ continues to increase but deviates significantly from C-W law. On further lowering of the temperature, $\varepsilon_r(T)$ shows a nearly temperature-independent plateau with a very high value of $\varepsilon_r \sim 25000$ in $SrTiO_3$ [10,27] and ∼4000 in $KTaO_3$ [28]. The $\omega_{TO}^2(T)$ also saturates to a rather low value which never goes to zero in the limit of $T \rightarrow 0$ K [23–25], suggesting the stabilization of the paraelectric state. Muller and Burkhard [10] attributed it to the zero-point fluctuations in the atomic positions of Ti^{4+} in the context of $SrTiO_3$ at low temperatures. They accordingly termed such compounds as quantum paraelectrics (QPE) [10], which may be regarded as being on the disordered side of the FE QCP. They used the quantum mechanical analog of Curie-Weiss law, commonly known as Barret's law [29], to explain the observed temperature dependence of the dielectric constant and its saturation below 4 K in $SrTiO_3$:

$$\varepsilon = \varepsilon_0 + M/[0.5T_1 \coth\,(T_1/2T) + T_0], \tag{1}$$

where M is related to dipole density, T_0 is like the C-W temperature, and T_1 is the crossover temperature from classical to quantum regime. Since then, a large number of quantum paraelectrics have been discovered with quantum saturation regime extending to much higher temperatures (upto ∼50 K) in some high-temperature quantum paraelectrics [30,31]) with both positive [10,32] and negative T_0 [30,32–36] corresponding to their incipient FE [13] and incipient antiferroelectric (AFE) [36] characters, respectively. The use of nonthermal control parameters (g), such as composition [36–38], electric field [39,40], and pressure [12,28], have been shown to drive these compounds to a quantum ferroelectric (QFE) state on the other side of a QCP with T_c varying as $(g - g_c)^{1/2}$ with a nonclassical exponent (1/2) in the QCR [11,13,37]. The so-called QFE state in Ca^{2+} doped $SrTiO_3$ [37] is now known to be a quantum ferrielectric state [41] which transforms to an unusual AFE phase at higher Ca^{2+} concentrations [42].

Barrett's law is a single-ion model corresponding to the soft TO branch in which each atom behaves as an independent Einstein oscillator in the presence of a small anharmonic term added to the potential energy. Recently, it has been shown [43] that the inverse of the dielectric susceptibility $[\chi_e(T)^{-1}]$ of QPEs, such as $SrTiO_3$ and $KTaO_3$, in the QCR exhibits an upturn with a T^2 dependence above the upturn temperature in disagreement with the dielectric plateau predicted by Barrett's law. The nonclassical exponent for $\chi_e(T)^{-1}$ above the upturn temperature is in agreement with the theoretical predictions for the multiaxial displacive FEs in the quantum limit taking into account the coupling of the soft dispersive TO branch with all other phonon branches in the anharmonic term [13,43–48] while the upturn in $\chi_e(T)^{-1}$ at low temperatures has been attributed to electrostrictive effects [43]. Since then, other magnetic QPEs, such as $BaFe_{12}O_{19}$ (BFO) [49] and $SrFe_{12}O_{19}$ (SFO) [49], have also been shown to exhibit similar upturns but with $\chi_e(T)^{-1}$ varying as T^3 above the upturn temperature, as expected for uniaxial displacive FEs in the quantum limit [44]. More recently, the quantum critical behavior of multiferroic systems, where the magnetic and FE QCPs can be tuned by some nonthermal control parameters, has also been discussed theoretically [50,51] with interesting predictions such as (1) the existence of a magnetically enhanced polar state that transforms to a reentrant QPE state on lowering the temperature at a constant value of the nonthermal control parameter, and (2) the critical exponents for $\chi_e(T)^{-1}$ of such multiferroic QFE phases can vary from 2 to ∼3/2 and 5/2 as the two QCPs approach each other with biquadratic and additional lower order couplings, respectively, between the magnetic and FE order parameter fields.

Here, we present the results of a comprehensive study of temperature dependence of the dielectric constant [which is essentially the dielectric susceptibility $\chi_e(T)$ in displacive FEs], under zero and nonzero magnetic fields (H), and ac magnetic susceptibility $\chi_m(T)$ in the temperature range 4–80 K on an M-type hexaferrite $SrFe_{12}O_{19}$ (SFO). We show here that the upturn in $\chi_e(T)^{-1}$ reported earlier [49] is due to a dipole glass (DG) transition, which is linked to a spin glass (SG) transition via magnetodielectric coupling of the two diverse order parameter fields. The ergodic symmetry-breaking temperatures for the dipole glass (T_{DG}) and spin glass (T_{SG}) transitions nearly coincide within ±1 K despite the large difference in the corresponding timescales for the electric dipole and spin dynamics suggesting SFO to exhibit a canonical multiglass state. This is in contrast to previously reported multiglass systems where T_{DG} and T_{SG} differ much more [52–55]. We also show that the dipole glass freezing temperature (T_{f1}) increases with magnetic field (H) at a constant frequency suggesting that it is a magnetically stabilized phase [50]. On lowering the temperature further below the DG transition, a reentrant QPE state appears [50], which can be transformed under dc magnetic field bias to another phase, most likely a second dipole glass phase as its freezing temperature (T_{f2}) also shifts to the higher temperature side with increasing frequency. Unlike the multiglass phase, this transition is not accompanied by any magnetic transition, and its freezing temperature T_{f2} decreases with increasing H, suggesting that it is destabilized by magnetic field. Finally, we show that near the dipole glass transition temperature without any dc magnetic field bias, $\chi_e(T)^{-1}$ shows an $\sim T^{5/2}$ dependence. Such a nonclassical exponent is indicative of multiferroic quantum criticality due to the usual biquadratic along with lower order magnetoelectric couplings of order parameter fields [50]. Evidence for such a coupling is also presented from a study of the variation of dielectric constant with magnetic field at 3 and 20 K. These results are discussed in the light of the recent theoretical work on multiferroic quantum criticality [50] and the future directions in which more theoretical efforts are required.

II. SYNTHESIS AND CHARACTERIZATION DETAILS

Strontium hexaferrite ($SrFe_{12}O_{19}$) samples were synthesized by the solid state thermochemical reaction route. Analytical reagent grade chemicals $SrCO_3$ (⩾99.0% assay; Sigma Aldrich) and Fe_2O_3 (⩾99.0% assay; Sigma Aldrich) were mixed in the stoichiometric ratio first using an agate mortar and pestle for 1 h followed by ball milling in a zirconia jar with zirconia balls for 12 h. Acetone was used as the grinding medium. The sample was dried after mixing at room temperature. The dried samples were calcined at 1200° C for 6 h. Then, pellets were made using cylindrical steel die and a uniaxial hydraulic press. $SrFe_{12}O_{19}$ (SFO) pellets were sintered at 1320° C for 3 h.

The phase purity of the sintered sample was first verified using x-ray diffraction (XRD) data obtained from an in-house 18-kW rotating anode-based diffractometer with a curved crystal monochromator in the diffraction beam (model No. RINT 2500/PC series; Rigaku). The room temperature synchrotron x-ray diffraction (SXRD) data were also collected at a wavelength of 0.20715 Å at the P02.1 beamline of Petra III, DESY, Hamburg, Germany. For XRD and SXRD measurements, sintered pellets were crushed into fine powders and annealed at 600° C for 10 h to remove any strains introduced during crushing. The XRD and SXRD data were collected on such annealed powder samples.

Capacitance measurements were carried out using an Alpha-A high frequency analyzer (Novocontrol Technologies, Germany), which can measure capacitance from 1 fF to 1 F and tanδ from 10^{-5} to 10^{4} with a resolution of $<10^{-5}$. For temperature-dependent capacitance measurements without and with magnetic field, a Cryogen Free 7 Tesla Measurement System (Cryogenic Limited, UK) with variable temperature insert was used. The sample temperature was controlled using a programmable temperature controller (Model: 350; Lake Shore Cryogenics) with temperature stability of ±2.4 mK between 3 and 100 K. The temperature of the sample was ramped at a constant rate of 0.4 K/min while frequency-dependent capacitance was measured in the presence/absence of magnetic field. Before the dielectric measurements, sintered pellets were first mildly polished using 25-μm diamond paste and electroded using fired-on silver paste. The capacitance and loss tangent were measured at 150 kHz in the 4–80 K range while frequency-dependent measurements, from 1 to 215 kHz, were carried out in the 4–40 K range. Temperature dependence of capacitance and loss tangent were measured at 150 kHz in the presence of varying magnetic fields (100–30 000 Oe) also in the 3–20 K temperature range. Magnetic ac susceptibility measurements were carried out on pieces of the sintered pellets using a physical property measurement system (DynaCool, Quantum Design).

III. RESULTS AND DISCUSSION

A. Phase purity and room temperature crystal structure of $SrFe_{12}O_{19}$

$SrFe_{12}O_{19}$ possesses magnetoplumbite structure at room temperature in the hexagonal space group $P6_3/mmc$ [56]. The unit cell of this structure contains two formula units of $SrFe_{12}O_{19}$. The two strontium (Sr^{2+}) ions occupy $2d$ and 24 iron (Fe^{3+}) ions are distributed over five distinct Wyckoff positions, $2b$ (trigonal bipyramid or TBP site), $4f_{\mathrm{iv}}$ (tetrahedral site), $2a$, $4f_{\mathrm{vi}}$, and $12k$ (octahedral site) while the 38 oxygen (O^{2-}) ions occupy five different sites, namely, $4e$, $4f$, $6h$, $12k$, and $12k$ [56]. To verify the phase purity and crystal structure of our SFO samples, we used SXRD data at room temperature. It was verified that all the peaks can be indexed using the magnetoplumbite structure. Rietveld refinement was carried out for determining the atomic positions of the asymmetric unit of the structure using SXRD data with the help of the FULLPROF suite [57]. In the refinement, the background was modeled using a six-order polynomial. The peak shape was modeled using a pseudo-Voigt function. The scale factor, FWHM parameters, zero displacement, lattice parameters, positional coordinates, and thermal parameters were refined while the occupancy of each ion was fixed at its nominal composition value. Atomic positions in the asymmetric unit of the hexagonal unit cell for the $P6_3/mmc$ space group used in refinements are (2/3,1/3,0.25) for Sr^{2+} at the $2d$ site, (0,0,0) for Fe^{3+} (Fe1) at the $2a$ site, (0,0,0.25) for Fe^{3+} (Fe2) at the $2b$ site, (1/3,2/3,z) for Fe^{3+} (Fe3) at the $4f_{\mathrm{iv}}$ site, (1/3,2/3,z) for Fe^{3+} (Fe4) at the $4f_{\mathrm{vi}}$ site, (x, $2x$, z) for Fe^{3+} (Fe5) at the $12k$ site, (0,0,z) for O1 at the $4e$ site, (1/3,2/3,z) for O2 at the $4f$ site, (x, $2x$,0.25) for O3 at the $6h$ site, (x, $2x$, z) for O4 at the $12k$ site, and (x, $2x$, z) for O5 at the $12k$ site. The refinement converged satisfactorily after a few cycles. The observed profile along with the calculated and the difference profiles obtained after the Rietveld refinement are shown in Fig. 1. The nearly flat difference profile suggests an excellent quality of fit between the observed and calculated profiles. Our Rietveld analysis of SXRD data confirms that our $SrFe_{12}O_{19}$ samples are monophasic with the magnetoplumbite structure in the $P6_3/mmc$ space group. The positional coordinates of the atoms in the asymmetric unit and the lattice parameters obtained after the Rietveld refinement are given in Table I.

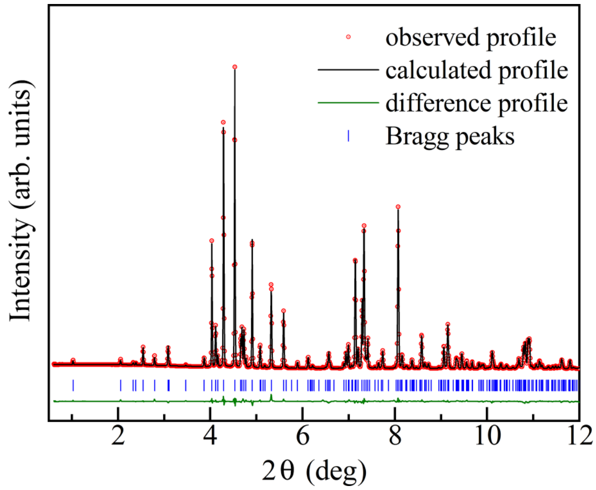

FIG. 1. The results of Rietveld refinement using the SXRD data on $SrFe_{12}O_{19}$ samples.

B. Confirmation of off-centered positions for the Fe^{3+} ion at the TBP site

Although the structure of $SrFe_{12}O_{19}$, like other M-type hexaferrites, is believed to be centrosymmetric in the space group $P6_3/mmc$, there are several studies [56,58–62] which suggest that the Fe^{3+} ion position at (0,0,0.25) on the mirror

TABLE I. Lattice parameters, positional coordinates, and thermal parameters of the atoms in the asymmetric unit of $SrFe_{12}O_{19}$ obtained from Rietveld refinement of the structure.

Atoms/coordinates	x	y	z	B_{iso}
Sr	2/3	1/3	0.25	0.0044(8)
Fe1	0	0	0	0.0049(1)
Fe2	0	0	0.25	0.0071(1)
Fe3	1/3	2/3	0.02742(1)	0.0057(8)
Fe4	1/3	1/3	0.19093(1)	0.0063(8)
Fe5	0.1688(4)	$2x$	−0.10875(6)	0.0054(5)
O1	0	0	0.1509(4)	0.005(3)
O2	1/3	2/3	−0.0546(4)	0.000(3)
O3	0.180(2)	$2x$	0.25	0.006(3)
O4	0.1554(2)	$2x$	0.0525(2)	0.0054(2)
O5	0.5020(2)	$2x$	0.1506(2)	0.0060(2)

$a = b = 5.88163(4)$ Å, $c = 23.0699(3)$ Å, $\chi^2 = 1.02$
$Fe_2{-}O_{ab} = 1.834(2)$, $Fe_2{-}O_{ap} = 2.2862(2)$

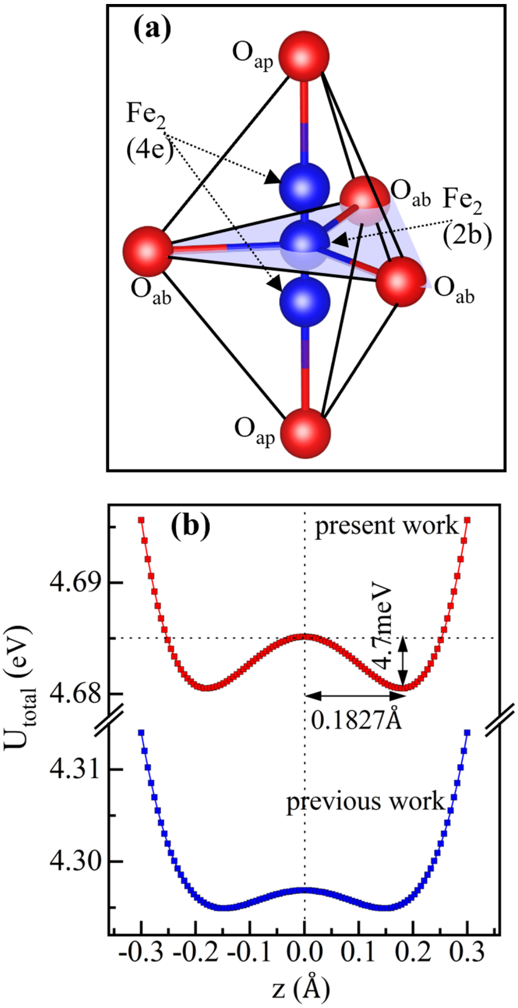

FIG. 2. (a) TBP polyhedra with the two off-centered positions ($4e$) of Fe^{3+} and (b) the double-well potential corresponding to the two off-centered positions.

plane passing through the center of the TBP [see Fig. 2(a)] is not stable. Recently, this has been demonstrated by potential energy calculations for the Fe^{3+} ion in the TBP coordination using nearest neighbor attractive Coulombic ($U_{\text{Coulombic}}$) and repulsive ($U_{\text{repulsion}}$) contributions [32], modeled using phenomenological potential terms as per the following expressions [63]:

$$U_{\text{total}}(z) = U_{\text{Coulomb}}(z) + U_{\text{repulsion}}(z), \tag{2}$$

where

$$U_{\text{Coulomb}}(z) = -\frac{3 \times 6e^2}{\sqrt{r_0^2 + z^2}} - \frac{6e^2}{r_1 + z} - \frac{6e^2}{r_1 - z}, \tag{3}$$

and

$$\begin{aligned} U_{\text{repulsion}}(z) = {} & 3\beta c_{+-} e^{(r_+ + r_- - \sqrt{r_0^2+z^2})/\rho} \\ & + \beta c_{+-} e^{[r_+ + r_- - (r_1+z)]/\rho} \\ & + \beta c_{+-} e^{[r_+ + r_- - (r_1-z)]/\rho}. \end{aligned} \tag{4}$$

Here, e is the electronic charge ($-2e$ for the O ion and $+3e$ for the Fe^{3+} ion), z is the off-center displacement of the Fe^{3+} ion away from the $2b$ Wyckoff site along the c axis, r_0 and r_1 are the Fe^{3+}-O_{ab} and Fe^{3+}-O_{ap} bond lengths in Å, respectively, shown in Fig. 2(a). The values of different parameters were fixed as $\beta = 1.35 \times 10^{-19}$ J, $c_{+-} = 1$(Pauling's valence factor), $r_+ = 1.4$ Å (ionic radii of O^{2-}), $r_- = 0.58$ Å (ionic radii of Fe^{3+}), and $\rho = 0.315$ [63]. The bond lengths used in Ref. [32] were taken from an old work [64], which differ slightly from those obtained from our Rietveld refined coordinates given in Table I. We have therefore recalculated the potential energy of the Fe^{3+} ion in the TBP coordination considering off-center displacements along the z axis perpendicular to the mirror plane passing through the center of the TBP. The calculated potential energy curve along with that obtained by the previous workers [32] is shown in Fig. 2(b). Our results are in agreement with the results of previous calculations [32] and hence further studies on our polycrystalline samples qualify to be compared with the earlier work. It is worth noting that the Fe^{3+} ions in the TBP coordination are off-centered and can occupy two symmetrically located degenerate positions in a double-well potential along the c axis (i.e., perpendicular to the mirror plane passing through the center of the TBP). Such an off-centering implies that the center of symmetry is broken locally giving rise to electric dipoles with moments pointing along or opposite to the c axis. The depth of the potential well is ~4.7 meV, which is much smaller than the available thermal energy ~25.8 meV at room temperature. Therefore, both minima are accessible with equal probability. The thermal energy decreases with temperature (~1.29 meV at 15 K) but this degeneracy in the position of the dipoles located in the double-well potential is not lifted globally even at the lowest temperatures, presumably because of the combined effect of thermal and quantum fluctuations leading to the stabilization of the quantum paraelectric state at low temperatures in SFO [32] preceded by a cluster dipole glass state.

C. Evidence for reentrant quantum paraelectric state

Recent experimental studies suggest that the M-type hexaferrites are uniaxial displacive incipient FEs/AFEs due to the off-center displacement of Fe^{3+} ions in the TBP coordination along the c axis [32] [see Fig. 2(a)] as a result of the softening of a zone center TO mode whose frequency remains nonzero down to 0 K [65]. However, the fact that Fe^{3+} ions in the TBP environment randomly occupy the minima in the double-well potential shown in Fig. 2(b), there is an order-disorder character also associated with the soft mode similar to $BaTiO_3$ where Ti^{4+} occupies eight equivalent local minima along the $\langle 111 \rangle$ directions in its cubic phase either due to its order-disorder character at low temperatures or due to large anharmonicity [26,66,67]. Since the $3d^5$ Fe^{3+} ion in the TBP contributes to both the magnetic moment and the local electric dipole moment, the M-type hexaferrites defy the usual $3d^0$ norm for ferroelectric off-center displacements in ABO_3 perovskites [68].

Figure 3(a) depicts the typical temperature dependence of the real [$\varepsilon'(T)$] and imaginary [$\varepsilon''(T)$] parts of the dielectric constant of SFO in the 4–80 K range, measured at 150 kHz

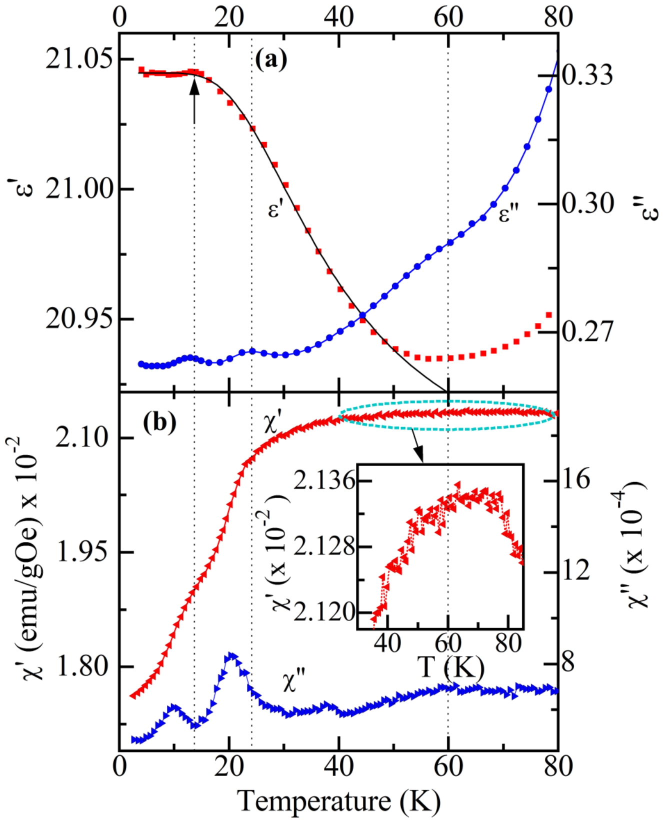

FIG. 3. (a) Plots of $\varepsilon'(T)$ and $\varepsilon''(T)$ at 150 kHz. (b) Plots of $\chi'_m(T)$ and $\chi''_{\rm m}(T)$ at 5 kHz. Solid black line through the $\varepsilon'(T)$ plot in (a) corresponds to the Barret's fit.

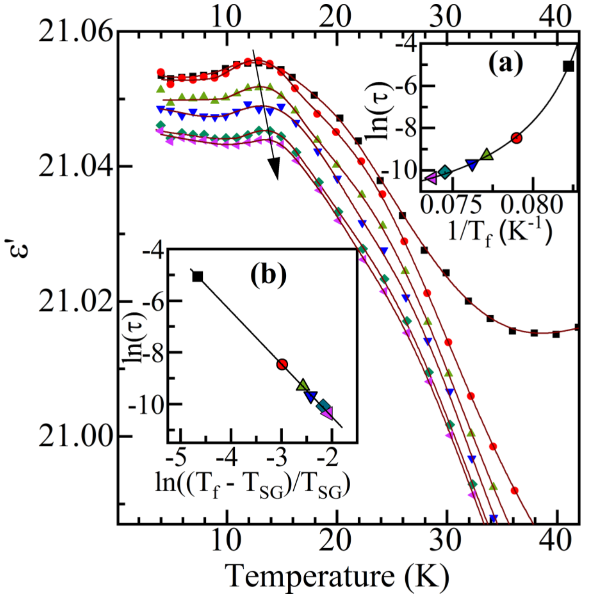

FIG. 4. Plot of $\varepsilon'(T)$ at various frequencies: ■, 1 kHz; •, 30 kHz; ▲, 70 kHz; ▼, 100 kHz; ♦, 150 kHz, and ◄, 200 kHz. Insets show (a) VF fit and (b) power-law fit for the relaxation time [$\tau(T)$].

on a silver-electroded high-density and well-characterized sintered pellet piece. The nature of the ε' (T) plot in Fig. 3(a) is similar to the $\varepsilon'_{\rm c}$ (T) plot for single crystals where Barrett's-like behavior along the c axis and nearly temperature-independent behavior of $\varepsilon'_{\rm ab}(T)\,[<\varepsilon'_c(T)]$ in the ab plane have been reported below 50 K [32]. The absolute value of $\varepsilon'(T)$ is somewhat reduced in the polycrystalline sample due to the averaging over the $\varepsilon'_{\rm c}$ and $\varepsilon'_{\rm ab}$ values in randomly oriented grains and slight uncertainty in the geometrical dimensions also. The increasing trend in $\varepsilon'(T)$ and $\varepsilon''(T)$ above ~60 K in Fig. 3(a) is due to conductivity losses, reported in single crystals also, as SFO is an n-type semiconductor with a rather small bandgap [69]. The Barrett's law [29] gives fairly satisfactory fit to the observed $\varepsilon'(T)$ below 50 K with $M = (1.59 \pm 0.01)$, $T_0 = (44.9 \pm 0.3)$ K, and $T_1 = (108.0 \pm 0.1)$ K, as can be seen from the continuous line in Fig. 3(a). The positive value of T_0 indicates the presence of ferroelectriclike correlations unlike the AFE correlations with negative T_0 reported for the isostructural BFO [22,32]. Although the values of these parameters naturally differ somewhat from those corresponding to the single-crystal values [32], they do indicate the QPE behavior at lower temperatures.

D. Evidence for dipole glass state preceding the reentrant QPE state

The first indication that something is amiss in the Barrett's fit in the quantum saturation regime comes from the temperature dependence of the imaginary part of the dielectric constant $\varepsilon''_{\rm r}(T)$, which surprisingly has not been given in the earlier reports [32,49]. The $\varepsilon''(T)$ plot in Fig. 3(a) shows a peak at around $T''_{\rm f1} \sim 12.8$ K related to a tiny peak in the $\varepsilon'(T)$ plot at $T'_{\rm f1} \sim 13.4$ K. Our $T'_{\rm f1}$ is close to the upturn temperature of ~14 K in $\chi_{\rm e}(T)^{-1}$ reported earlier [49]. The second peak in the $\varepsilon''(T)$ plot at $T''_{\rm f1} \sim 24$ K does not lead to any obvious anomaly in the $\varepsilon'(T)$ plot. The tiny peak at ~13.4 K for 150 kHz is not accounted for by Barrett's law. It precedes the onset of a nearly temperature-independent plateau region of the $\varepsilon'(T)$ plot at lower temperatures indicating the emergence of a reentrant QPE state of SFO predicted theoretically for multiferroic quantum criticality [50]. It is worth noting that the peak in the $\varepsilon''(T)$ plot occurs at a slightly lower temperature ($T''_{\rm f1} = 12.8$ K) than the peak in $\varepsilon'(T)$ ($T'_{\rm f1} = 13.4$ K) in Fig. 3(a). This is unlike that for a regular long-range ordered polar transition, for which $T'_{\rm f1}$ must be equal to $T''_{\rm f1}$ as per the Kramer-Kronig relationship [26]. For DG [as also for relaxor ferroelectric (RFE)] transitions, on the other hand, $T''_{\rm f1}$ is known to be less than $T'_{\rm f1}$ [22,70]. The frequency-dependent $\varepsilon'(T)$ response, measured over a 4–40 K temperature range, reveals that $T'_{\rm f1}$ shifts to higher temperatures with increasing value of the measuring frequency ($f = \omega/2\pi$; see Fig. 4), similar to DG [71,72] and RFE [70,73,74] transitions. The dipolar relaxation time (τ) was obtained from the $\omega\tau = 1$ relationship for each temperature $T'_{\rm f}(\omega)$ [73,74]. The noncritical slowing down of the dipolar dynamics is usually modeled using the Arrhenius relationship where τ follows the temperature dependence

$$\tau = \tau_0 \exp{(E_{\rm a}/k_{\rm B}T)}, \tag{5}$$

where τ_0 is the inverse of the attempt frequency or the attempt relaxation time while $E_{\rm a}$ is the activation energy for the dipole relaxation process in the double-well potential and $k_{\rm B}$ is the Boltzmann constant. For such a noncritical temperature-dependent behavior of τ, the $\ln(\tau)$ versus $1/T_f'$ plot should have been linear. However, as can be seen from the inset "(a)" of Fig. 4, this plot is nonlinear. This is a typical characteristic of DGs [71,72] and RFEs [70,73,74], where the temperature dependence of the relaxation time τ has been analyzed in terms of Vogel-Fulcher (VF) [70,73] and power-law [52] behaviors, in analogy with the SG systems [75] given below:

$$\tau = \tau_0 \exp\left[E_a/k_B(T - T_{VF})\right] \tag{6}$$

and

$$\tau = \tau_0[(T_f - T_{DG})/T_{DG}]^{z\upsilon}, \tag{7}$$

where T_{VF} and T_{DG} are the characteristic temperatures at which the slowest dipolar dynamics diverges signaling the breaking of the ergodic symmetry. The $z\upsilon$ is the dynamical critical exponent related to the correlation length [75]. The fit between the observed and calculated temperature dependence of τ for both VF and power laws are quite satisfactory, as can be seen from the insets (a) and (b) of Fig. 4, respectively, with the least-squares fitting parameters $z\upsilon = (2.04 \pm 0.01)$, $\tau_0 = (4.7 \pm 0.2) \times 10^{-7}$ s and $T_{DG} = (12.05 \pm 0.01)$ K for the power law and $E_a = 0.46$ meV, $\tau_0 = (2.5 \pm 0.1) \times 10^{-6}$ s, and $T_{VF} = (11.48 \pm 0.01)$ K for the VF law. The activation energy E_a for dipoles thus obtained is one order of magnitude smaller than the potential well shown in Fig. 2(b). The relatively large value of τ_0 indicates the presence of clusters of correlated dipoles with frustrated intercluster interactions similar to cluster spin glasses [75]. Further, the ergodic symmetry-breaking temperatures for the DG state for the two laws are very close to each other with $T_{DG} \sim 12$ K and $T_{VF} \sim 11.5$ K.

E. Evidence for the multiglass character of the dipole glass state

The ac magnetic susceptibility $\chi_m'(T)$ plot shown in Fig. 3(b) reveals two relaxation steps at ~13.4 and ~24 K, which correlate well with the peak temperatures T_{f1}' (150 kHz) = 13.4 K and T_{f2}'' (150 kHz) = 24 K in the $\varepsilon'(T)$ and $\varepsilon''(T)$ plots in Fig. 3(a). Such a correlation between the magnetic and dipole glass transitions was missed in the previous studies [32,49]. Interestingly, even the hump in the $\varepsilon''(T)$ plot around 55 K correlates well with a weak magnetic anomaly shown more clearly in the inset of Fig. 3(b). We find that similar to $BaFe_{12}O_{19}$ [76–78], SFO undergoes a succession of SG transitions below room temperature but the details of all these transitions is outside the scope of the present report. We shall focus only on the lowest temperature relaxation step in the $\chi_m'(T)$ plot shown in Fig. 3(b) which correlates with the DG transition in the $\varepsilon'(\omega,T)$ plot of Fig. 4. Since it was not possible to extract the information about SG freezing temperatures $T_f'(\omega)$ from the $\chi_m'(T)$ plot [see Fig. 3(b)] reliably, we analyzed the frequency dependence of the upturn temperature in $\chi_m''(T)$, which is known to coincide with $T_f'(\omega)$ for SG systems [75,79], as can be seen from the first dotted line in Fig. 3(b). This is because the onset of an increase in dissipation revealed by $\chi_m''(\omega,T)$ in glassy systems coincides with the onset of glassy freezing at $T_f'(\omega)$ revealed by the peak in the $\chi_m'(\omega,T)$ plot. The frequency dependence of the upturn temperature in the $\chi''(\omega,T)$ plot is shown in Fig. 5(a) and the results of its analysis in terms of power-law and VF relationships given by Eqs. (7) and (6), are shown in Fig. 5(b) and its inset, respectively. Both analyses confirm the existence of a critical temperature, $T_{SG} = (11.05 \pm 0.01)$ K and $T_{VF} = (10.66 \pm 0.02)$ K, at which the ergodic symmetry is broken with the divergence of $\tau(T)$ for the fitting parameters: $z\upsilon = (0.84 \pm 0.02)$, $\tau_0 = (4.7 \pm 0.3) \times 10^{-3}$ s and $E_a = 0.11$ meV, $\tau_0 = (1.25 \pm 0.05) \times 10^{-2}$ s, respectively. Interestingly, the ergodicity breaking temperatures for the DG and SG transitions nearly coincide ($T_{DG} \sim T_{SG}$) within ±1 K. All these results indicate that $SrFe_{12}O_{19}$ exhibits a canonical multiglass state, preceding the onset of the quantum paraelectric (QPE) saturation of $\varepsilon'(T)$, with near coincidence of T_{DG} and T_{SG}, unlike the previous reports where the two characteristic temperatures differ much more [52–55].

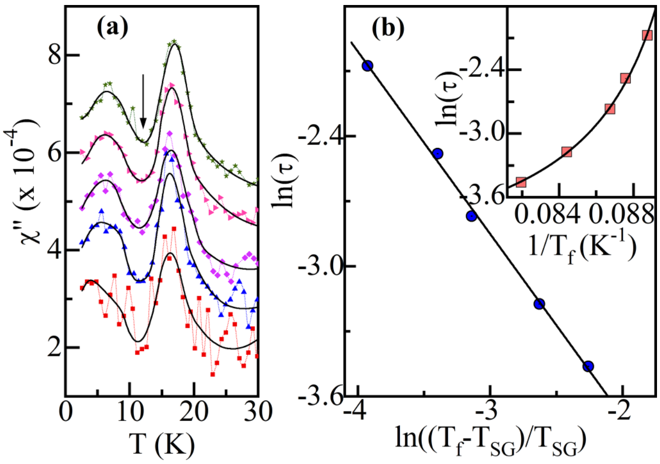

FIG. 5. (a) Plot of $\chi_m''(T)$ at various frequencies: ■, 50 Hz; ▲, 75 Hz; ♦, 100 Hz; ▶, 150 Hz; ★, 200 Hz. For clarity each curve is shifted by a constant value 8×10^{-5}. Black solid line through the data points is a guide to the eyes. (b) The power-law and VF law fits (inset) for the relaxation time τ at each T_f obtained from the upturn point marked with an arrow in (a).

F. Effect of magnetic field on reentrant quantum paraelectric and multiglass state

The multiglass of $SrFe_{12}O_{19}$ is sensitive to perturbations caused by dc magnetic field (H) as can be seen from Fig. 6(a), which depicts $\varepsilon'(T)$ plots measured at 150 kHz under various H in the range 100–30 000 Oe. In addition, Fig. 6(a) also reveals that the reentrant QPE state is destabilized by the magnetic field. As is evident from the figure, even a small magnetic field of 100 Oe is sufficient to suppress the quantum fluctuations in the reentrant QPE state and stabilize a lower temperature phase with a second peak in $\varepsilon'(T)$ at ~7.9 K. The transition temperature corresponding to this phase is found to decrease nonmonotonically with increasing magnetic field [see inset of Fig. 6(b)] raising the possibility of approaching a QCP as a function of magnetic field at much higher magnetic fields. In sharp contrast to the transition induced by dc magnetic field in the reentrant QPE state, the multiglass freezing temperature T_{f1} increases nonmonotonically with increasing field, as can be seen from Fig. 6(b). It is interesting to note that the DG character of the higher temperature transition around 13.4 K is retained under dc magnetic field bias as it

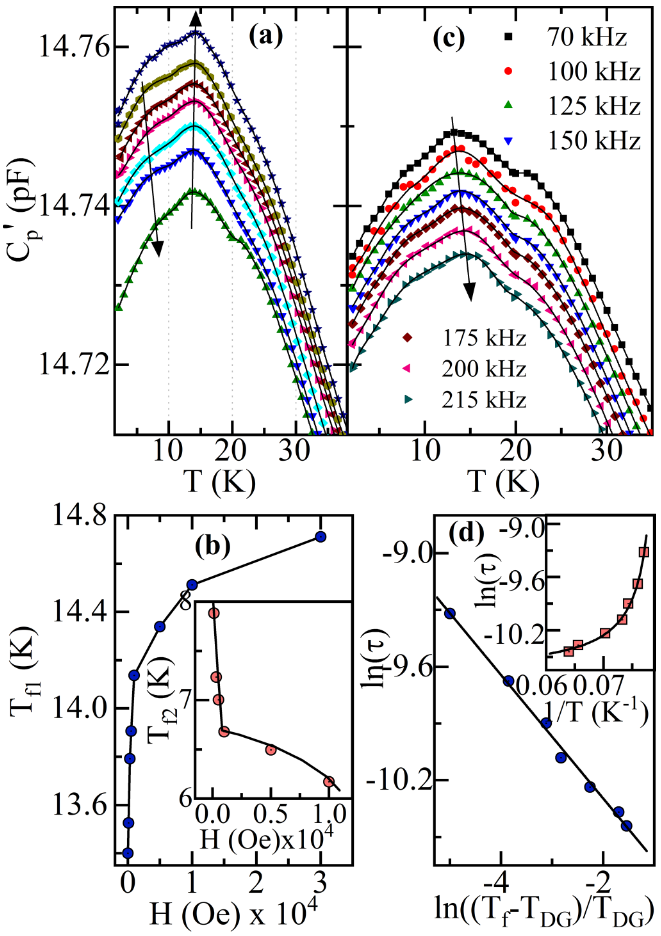

FIG. 6. (a) Variation of capacitance C_P' with T at 150 kHz measured under dc magnetic fields, where the arrows passing through the freezing temperatures T_{f1} and T_{f2} are guides to the eyes: $H =$ ▲, 100 Oe; ▼, 300 Oe; ◆, 500 Oe; ▶, 1000 Oe; ◀, 5000 Oe; ⬢:10 000 Oe; ★, 30 000 Oe. (b) Variation of T_{f1} and T_{f2} with field (H). (c) $C_P'(\omega, T)$ measured at various frequencies at $H = 100$ Oe. (d) Power-law fit with $T_{DG} \sim (12.88 \pm 0.01)$ K, $z\upsilon = (0.32 \pm 0.01)$, and $\tau_0 = (1.07 \pm 0.05) \times 10^{-5}$ s. Inset of (d) shows VF law fit with $T_{VF} \sim (12.42 \pm 0.02)$ K, $\tau_0 = (2.41 \pm 0.04) \times 10^{-5}$ s, and $E_a = 0.061$ meV.

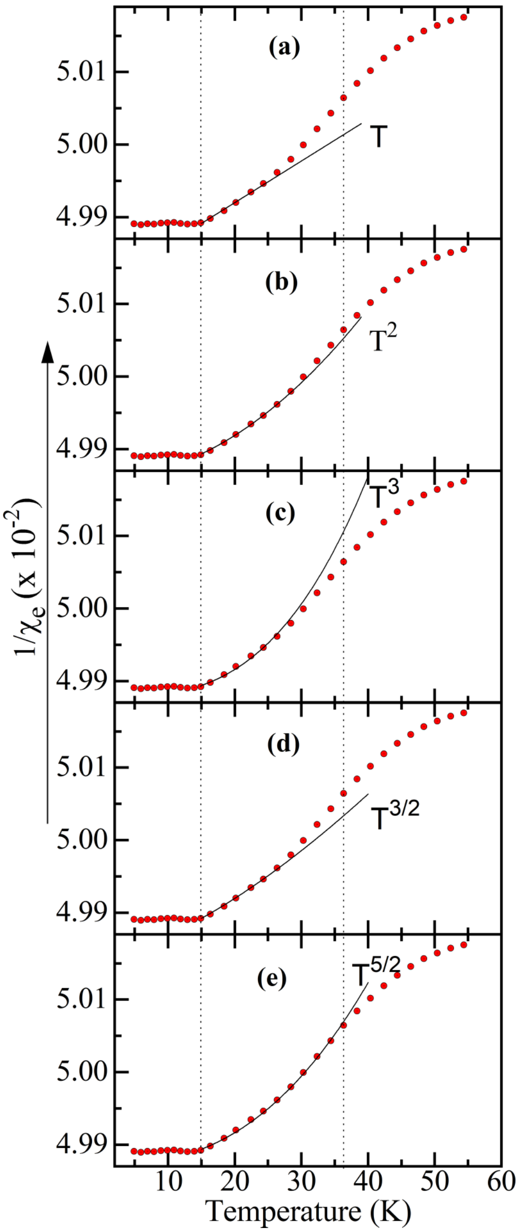

FIG. 7. Inverse dielectric susceptibility $(1/\chi_e)$ vs T with fits for various critical exponents $n =$(a) 1, (b) 2, (c) 3, (d) 3/2, and (e) 5/2 in the 15–36 K range.

continues to show the characteristic shift in $T_f^{'}(\omega)$ towards the higher temperature side on increasing the frequency as shown in Fig. 6(c). Excellent least-squares fits for the VF and power laws were obtained using Eqs. (6) and (7) as can be seen from the inset and the main panel of Fig. 6(d), respectively. The corresponding ergodic symmetry-breaking temperatures are $T_{VF} \sim (12.42 \pm 0.02)$ K and $T_{DG} \sim (12.88 \pm 0.01)$ K, respectively. The frequency dispersion in the $T_f^{'}(\omega)$ of the lower temperature transition also points towards its DG character but it could not be confirmed due to the uncertainty in the location of the peak temperatures.

G. Evidence for nonclassical exponent

As stated earlier, the tiny peak in the $\varepsilon'(T)$ plot in Figs. 3(a) and 4 has been previously analyzed [49] in terms of quantum critical models for uniaxial ferroelectrics [44] in the 20–35 K range [49]. However, the basis of lower cut-off temperature is somewhat tentative as there is no estimate of the nonzero gap at the zone center for the soft TO mode of SFO unlike BFO [65]. More significantly, since we are dealing with a multiferroic multiglass transition, which can be further stabilized by magnetic field as evidenced by the increase in $T_f^{'}$ shown in Fig. 6(b), the multiferroic quantum critical models are required [50,51]. The presence of a reentrant QPE state in SFO below a magnetically enhanced DG state is consistent with the predictions of the multiferroic quantum criticality [50]. The temperature dependence of the inverse of the dielectric susceptibility $[\chi_e(T)^{-1}]$ was analyzed in terms of T^n−type dependence in the QCR. To obtain the critical exponent, we have used $1/\chi_e$ using the $\varepsilon'(150\ \text{kHz}, T)$ data. We have fitted the $1/\chi_e$ vs T plot in the temperature range 15–36 K

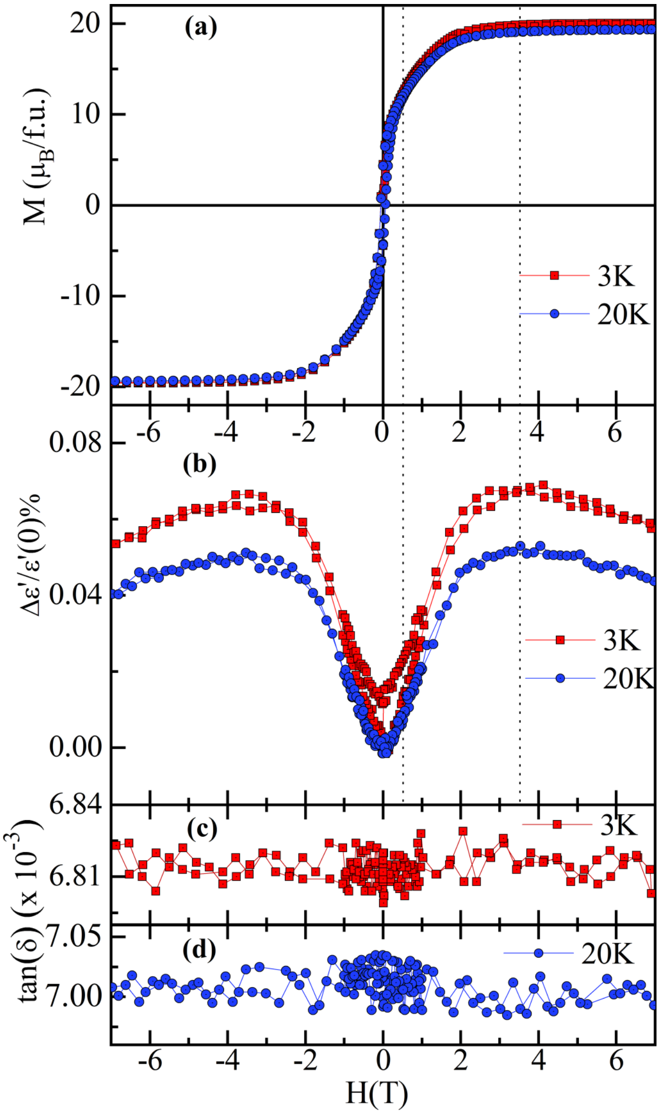

FIG. 8. Variation of (a) magnetization (M), (b) percentage change in dielectric constant percentage $\Delta\varepsilon'/\varepsilon'(H=0)$, and (c),(d) loss tangent (tanδ) as a function of magnetic field (H) measured at 3 and 20 K.

using $\sim T^{n}-$type dependence with exponents $n = 1{,}2{,}3$ [see Figs. 7(a)–7(c)] for the classical FE C-W law, quantum critical multiaxial FE model [43], and quantum critical uniaxial FE model [44,80]. An exponent 3/2 is predicted for the multiferroic quantum critical model when the FE and magnetic QCPs coincide with the usual biquadratic coupling of the two order parameter fields [50]. Inclusion of lower order coupling along with biquadratic coupling in the same multiferroic quantum critical model leads to an exponent of 5/2 [50] for $z = 2$. The corresponding fits for the multiferroic quantum critical models are depicted in Figs. 7(d) and 7(e). It is evident from Fig. 7, the best fit is obtained for $n\sim 5/2$, which covers the entire curvature of the $\chi_e(T)^{-1}$ curve in the temperature range 15–36 K, as can be seen from Fig. 7(e). This exponent is obviously a nonclassical exponent and may involve the effect of biquadratic and lower order magnetoelectric couplings in SFO.

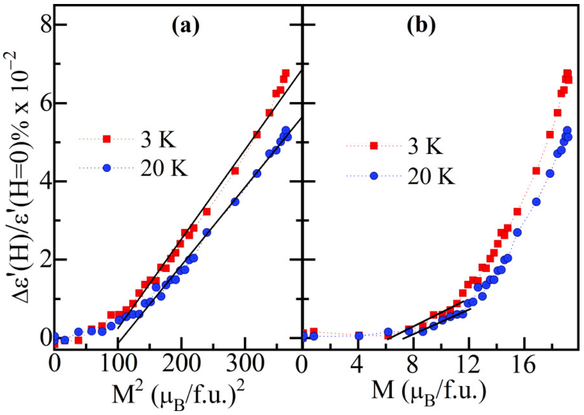

FIG. 9. The percentage change in ε' under dc magnetic field bias versus (a) M^2 and (b) M plots at 3 and 20 K.

To explore the nature of order parameter field couplings in SFO, the dc magnetization (M), ε', and dielectric loss tangent (tanδ) were measured as a function of field at 20 and 3 K following the approach discussed in the literature [81,82]. Using the $\varepsilon'(150\,\text{kHz}, H)$ data, the percentage change in ε', i.e., $\%\ \Delta\varepsilon'/\varepsilon'(H=0)$, where $\Delta\varepsilon' = \varepsilon'(H) - \varepsilon'(H=0)$, was calculated for different H. The field-dependent variation of M, $\%\ \Delta\varepsilon'/\varepsilon'(H=0)$ and tan(δ) are shown in Fig. 8. The percentage change in the dielectric constant $\varepsilon'(H)$ with respect to $\varepsilon'(H=0)$ increases with H prior to the saturation of magnetization but begins to decrease with a further increase in H in the saturation regime showing positive and negative magnetodielectric couplings, respectively (see Fig. 8). The magnetic field independence of the tan(δ) in this figure confirms that the magnetodielectric coupling is not due to magnetoresistance effects, as per the criterion outlined in Ref. [83]. The maximum change in the dielectric constant $\varepsilon'(H)$ due to the applied magnetic field is ∼0.06%, which is nearly half of that in multiferroic QPEs like EuTiO_3 [84] but is comparable to that in NiCr_2O_4 and Mn_3O_4 [82,85]. To unravel the order of magnetodielectric coupling in SFO, using M-H data [Fig. 8(a)] we have obtained the value of M using a linear interpolation method for all H at which the $\%\ \Delta\varepsilon'/\varepsilon'(H=0)$ has been measured. The $\%\ \Delta\varepsilon'/\varepsilon'(H=0)$ plotted against M^2 [81,82] is linear above $12\,\mu_B/\text{f.u.}$ at both 3 and 20 K [see Fig. 9(a)]. While the variation of the $\%\Delta\varepsilon'/\varepsilon'(H=0)$ for SFO shows the M^2 dependence at higher fields, consistent with the predictions for biquadratic order parameter couplings [Ref. [81] and see Fig. 9(a)], it also shows a departure from the M^2 dependence at lower fields possibly due to the presence of lower order couplings. Below $12\,\mu_B/\text{f.u.}$, a nearly linear variation between the $\%\ \Delta\varepsilon'/\varepsilon'(H=0)$ and M is observed as can be seen from Fig. 9(b). We believe that the magnetodielectric coupling is responsible for the appearance of the multiglass state of SFO and multiferroic quantum critical exponents.

IV. SUMMARY

To summarize, we have presented evidence for a reentrant QPE state preceded by a dipole glass transition with a nonclassical exponent (∼5/2) in the quantum critical regime of

$SrFe_{12}O_{19}$. The DG transition is accompanied with a spin glass transition characteristic of a canonical multiglass state in which the two diverse ergodic symmetry-breaking temperatures nearly coincide ($T_{DG} \sim T_{SG}$) within ±1 K due to magnetodielectric coupling. Further, we have shown that application of an external magnetic field can induce another transition, most likely a second DG transition, in the reentrant QPE state. The nature of this lower temperature transition is different from the higher temperature multiglass transition as it is not accompanied by any magnetic transition. Since its transition temperature decreases with increasing magnetic field, it shows the possibility of locating a polar QCP in $SrFe_{12}O_{19}$ at much higher magnetic fields than that used in the present work. The freezing temperature of the higher temperature dipole glass state, on the other hand, increases with the magnetic field, i.e., it is magnetically enhanced. While the observation of a reentrant QPE state and a magnetically enhanced DG state bears broad phenomenological similarities with the theoretical predictions for the multiferroic quantum critical model [50], there is obviously a need for developing a quantum critical model for a multiglass state with nearly coincident critical ergodic symmetry-breaking temperatures ($T_{DG} \sim T_{SG}$). We believe our findings will stimulate further experimental and theoretical studies on quantum critical multiferroic glassy systems.

ACKNOWLEDGMENTS

Financial support by the Department of Science and Technology (DST), Government of India provided within the framework of the India@DESY collaboration is gratefully acknowledged. The authors acknowledge DESY (Hamburg, Germany), a member of the Helmholtz Association HGF, for the provision of experimental facilities. K.K. is grateful to Prof. Premkumar Senguttuvan from JNCASR, Bengaluru for his support and encouragement.

---

[1] S. Sachdev, *Quantum Phase Transitions*, 2nd ed. (Cambridge University Press, Cambridge, 2011).
[2] M. Vojta, Frustration and quantum criticality, Rep. Prog. Phys. **81**, 064501 (2018).
[3] L. Savary and L. Balents, Quantum spin liquids: A review, Rep. Prog. Phys. **80**, 016502 (2017).
[4] P. Chandra, G. G. Lonzarich, S. E. Rowley, J. F. Scott, P. Jiang, and X. Huang, Prospects and applications near ferroelectric quantum phase transitions: A key issues review, Rep. Prog. Phys. **80**, 112502 (2017).
[5] T. Serwatka, R. G. Melko, A. Burkov, and P. N. Roy, Quantum phase transition in the one-dimensional water chain, Phys. Rev. Lett. **130**, 026201 (2023).
[6] M. Fellner, A. Messinger, K. Ender, and W. Lechner, Universal parity quantum computing, Phys. Rev. Lett. **129**, 180503 (2022).
[7] C. Noel *et al.*, Measurement-induced quantum phases realized in a trapped-ion quantum computer, Nat. Phys. **18**, 760 (2022).
[8] D. M. Broun, What lies beneath the dome? Nat. Phys. **4**, 170 (2008).
[9] M. Greiner, O. Mandel, T. Esslinger, T. W. Haensch, and I. Bloch, Quantum phase transition from a superfluid to a Mott insulator in a gas of ultracold atoms, Nature (London) **415**, 39 (2002).
[10] K. A. Muller and H. Burkard, $SrTiO_3$: An intrinsic quantum paraelectric below 4 K, Phys. Rev. B **19**, 3593 (1979).
[11] U. T. Hochli, Experimental studies on quantum ferroelectrics, Ferroelectrics **35**, 17 (1981).
[12] G. A. Samara, Quantum effects and glass-like behavior in ferroelectric oxides, Physica B (Amsterdam, Neth.) **150**, 179 (1988).
[13] O. E. Kvyatkovski, Quantum effects in incipient and low-temperature ferroelectrics (a review), Physica Solid State **43**, 1401 (2001).
[14] Y. Zheng *et al.*, Electrical property enhancement in orientation-modulated perovskite La-doped $SrTiO_3$, Adv. Funct. Mater. **33**, 2301815 (2023).
[15] A. A. Sirenko, C. Bernhard, A. Golnik, A. M. Clark, J. Hao, W. Si, and X. X. Xi, Soft-mode hardening in $SrTiO_3$ thin films, Nature (London) **404**, 373 (2000).
[16] I. A. Akimov, A. A. Sirenko, A. M. Clark, J. H. Hao, and X. X. Xi, Electric-field-induced soft-mode hardening in $SrTiO_3$ films, Phys. Rev. Lett. **84**, 4625 (2000).
[17] D. E. Kotecki *et al.*, $(Ba,Sr)TiO_3$ dielectrics for future stacked-capacitor DRAM, IBM J. Res. Dev. **43**, 367 (1999).
[18] B. Cheng, P. L. Kramer, Z. Shen, and M. C. Hoffmann, Terahertz-driven local dipolar correlation in a quantum paraelectric, Phys. Rev. Lett. **130**, 126902 (2023).
[19] C. Collignon, X. Lin, C. W. Rischau, B. Fauqué, and K. Behnia, Metallicity and superconductivity in doped strontium titanate, Annu. Rev. Condens. Matter Phys. **10**, 25 (2019).
[20] X. Li, T. Qiu, J. Zhang, E. Baldini, J. Lu, A. M. Rappe, and K. A. Nelson, Terahertz field–induced ferroelectricity in quantum paraelectric $SrTiO_3$, Science **364**, 1079 (2019).
[21] S.-P. Shen, J. Wu, J. Song, X. Sun, Y. Yang, Y.-S. Chai, D.-S. Shang, S.-G. Wang, J. F. Scott, and Y. Sun, Quantum electric-dipole liquid on a triangular lattice, Nat. Commun. **7**, 10569 (2016).
[22] K. Kumar and D. Pandey, Quantum phase transition in $Ba_{(1-x)}Ca_xFe_{12}O_{19}$ ($0 \leqslant x \leqslant 0.10$), Phys. Rev. B **96**, 024102 (2017).
[23] J. M. Worlock and P. A. Fleury, Electric field dependence of optical-phonon frequencies, Phys. Rev. Lett. **19**, 1176 (1967).
[24] P. A. Fleury and J. M. Worlock, Electric-field-induced Raman effect in paraelectric crystals, Phys. Rev. Lett. **18**, 665 (1967).
[25] J. F. Scott, Soft-mode spectroscopy: Experimental studies of structural phase transitions, Rev. Mod. Phys. **46**, 83 (1974).
[26] M. E. Lines and A. M. Glass, *Principle and Application of Ferroelectrics and Related Materials*, 1st ed. (Clarendon, Oxford, 1977).
[27] H. Uwe and T. Sakudo, Stress-induced ferroelectricity and soft phonon modes in $SrTiO_3$, Phys. Rev. B **13**, 271 (1976).
[28] G. A. Samara and B. Morosin, Anharmonic effects in $KTaO_3$: Ferroelectric mode, thermal expansion, and compressibility, Phys. Rev. B **8**, 1256 (1973).
[29] J. H. Barrett, Dielectric constant in perovskite type crystals, Phys. Rev. **86**, 118 (1952).
[30] P. H. Sun, T. Nakamura, Y. J. Shan, Y. Inaguma, and M. Itoh, High temperature quantum paraelectricity in perovskite-type

titanates $Ln_{1/2}Na_{1/2}TiO_3$ (Ln = La, Pr, Nd, Sm, Eu, Gd and Tb), Ferroelectrics **200**, 93 (1997).

[31] C. Ang, A. S. Bhalla, and L. E. Cross, Dielectric behavior of paraelectric $KTaO_3$, $CaTiO_3$, and $(Ln_{1/2}Na_{1/2})TiO_3$ under a dc electric field, Phys. Rev. B **64**, 184104 (2001).

[32] S.-P. Shen, Y. Chai, J. Cong, P. Sun, J. Lu, L. Yan, S. Wang, and Y. Sun, Magnetic-ion-induced displacive electric polarization in FeO_5 bipyramidal units of $(Ba, Sr)Fe_{12}O_{19}$ hexaferrites, Phys. Rev. B **90**, 180404(R) (2014).

[33] I. S. Kim, M. Itoh, and T. Nakamura, Electrical conductivity and metal-nonmetal transition in the perovskite-related layered system $Ca_{(n+1)}Ti_nO_{(3n+1-d)}$ ($n = 2$, 3 and ∞), J. Solid State Chem. **101**, 77 (1992).

[34] V. V. Lemanov, A. V. Sotnikov, E. P. Smirnova, and M. Weihnacht, From incipient ferroelectricity in $CaTiO_3$ to real ferroelectricity in $Ca_{1-x}Pb_xTiO_3$ solid solutions, Appl. Phys. Lett. **81**, 886 (2002).

[35] V. V. Lemanov, A. V. Sotnikov, E. P. Smirnova, M. Weihnacht, and R. Kunze, Perovskite $CaTiO_3$ as an incipient ferroelectric, Solid State Commun. **110**, 611 (1999).

[36] A. Chandra, R. Ranjan, D. P. Singh, N. Khare, and D. Pandey, The effect of Pb^{2+} substitution on the quantum paraelectric behaviour of $CaTiO_3$, J. Phys.: Condens. Matter **18**, 2977 (2006).

[37] J. G. Bednorz and K. A. Muller, $Sr_{1-x}Ca_xTiO_3$: An *XY* quantum ferroelectric with transition to randomness, Phys. Rev. Lett. **52**, 2289 (1984).

[38] M. Itoh, R. Wang, Y. Inaguma, T. Yamaguchi, Y. J. Shan, and T. Nakamura, Ferroelectricity induced by oxygen isotope exchange in strontium titanate perovskite, Phys. Rev. Lett. **82**, 3540 (1999).

[39] J. Dec, W. Kleemann, and B. Westwanski, Scaling behaviour of strontium titanate, J. Phys.: Condens. Matter **11**, L379 (1999).

[40] C. Ang, R. Quo, A. S. Bhalla, and L. E. Cross, Effect of electric field and post-treatment on dielectric behavior of $SrTiO_3$ single crystal, J. Appl. Phys. **87**, 3937 (2000).

[41] S. K. Mishra and D. Pandey, Low temperature x-ray diffraction study of the phase transitions in $Sr_{1-x}Ca_xTiO_3$ ($x = 0.02$,0.04): Evidence for ferrielectric ordering, Appl. Phys. Lett. **95**, 232910 (2009).

[42] R. Ranjan, D. Pandey, and N. P. Lalla, Novel features of $Sr_{1-x}Ca_xTiO_3$ phase diagram: Evidence for competing antiferroelectric and ferroelectric interactions, Phys. Rev. Lett. **84**, 3726 (2000).

[43] S. E. Rowley, L. J. Spalek, R. P. Smith, M. P. M. Dean, M. Itoh, J. F. Scott, G. G. Lonzarich, and S. S. Saxena, Ferroelectric quantum criticality, Nat. Phys. **10**, 367 (2014).

[44] D. E. Khmelnitskii and V. L. Shneerson, Low-temperature displacement-type phase transition in crystals, Sov. Phys. JETP **13**, 687 (1971).

[45] A. I. Larkin and D. E. Khmelnitskii, Phase transition in uniaxial ferroelectrics, Sov. Phys. JETP **29**, 43 (1969).

[46] R. Roussev and A. J. Millis, Theory of the quantum paraelectric-ferroelectric transition, Phys. Rev. B **67**, 014105 (2003).

[47] N. Das and S. G. Mishra, Fluctuations and criticality in quantum paraelectrics, J. Phys.: Condens. Matter **21**, 095901 (2009).

[48] L. Pálová, P. Chandra, and P. Coleman, Quantum critical paraelectrics and the Casimir effect in time, Phys. Rev. B **79**, 075101 (2009).

[49] S. E. Rowley, Y.-S. Chai, S.-P. Shen, Y. Sun, A. T. Jones, B. E. Watts, and J. F. Scott, Uniaxial ferroelectric quantum criticality in multiferroic hexaferrites $BaFe_{12}O_{19}$ and $SrFe_{12}O_{19}$, Sci. Rep. **6**, 25724 (2016).

[50] A. Narayan, A. Cano, A. V. Balatsky, and N. A. Spaldin, Multiferroic quantum criticality, Nat. Mater. **18**, 223 (2019).

[51] N. Das, Quantum critical behavior of a magnetic quantum paraelectric, Phys. Lett. A **376**, 2683 (2012).

[52] V. V. Shvartsman, S. Bedanta, P. Borisov, W. Kleemann, A. Tkach, and P. M. Vilarinho, (Sr,Mn)TiO_3: A magnetoelectric multiglass, Phys. Rev. Lett. **101**, 165704 (2008).

[53] K. Singh, A. Maignan, C. Simon, S. Kumar, C. Martin, O. Lebedev, S. Turner, and G. Van Tendeloo, Magnetodielectric $CuCr_{0.5}V_{0.5}O_2$: An example of a magnetic and dielectric multiglass, J. Phys.: Condens. Matter **24**, 226002 (2012).

[54] D. Choudhury *et al.*, Near-room-temperature colossal magnetodielectricity and multiglass properties in partially fisordered La_2NiMnO_6, Phys. Rev. Lett. **108**, 127201 (2012).

[55] S. Sharma, T. Basu, A. Shahee, K. Singh, N. P. Lalla, and E. V. Sampathkumaran, Multiglass properties and magnetoelectric coupling in the uniaxial anisotropic spin-cluster-glass Fe_2TiO_5, Phys. Rev. B **90**, 144426 (2014).

[56] X. Obradors, X. Solans, A. Collomb, D. Samaras, J. Rodriguez, M. Pernet, and M. Font-Altaba, Crystal structure of strontium hexaferrite $SrFe_{12}O_{19}$, J. Solid State Chem. **72**, 218 (1988).

[57] J. Rodríguez-Carvajal, FullProf, 2023, http://www.ill.eu/sites/fullprof/.

[58] J. Muller and A. Collomb, A new representation of the bipyramidal site in the $SrFe_{12}O_{19}$ M-type hexagonal ferrite between 4.6 and 295 K, J. Magn. Magn. Mater. **103**, 194 (1992).

[59] J. Fontcuberta and X. Obradors, Dynamics of the bipyramidal ions in $SrFe_{12}O_{19}$ studied Mossbauer spectroscopy, J. Phys. C: Solid State Phys. **21**, 2335 (1988).

[60] X. Obradors, A. Collomb, M. Pernet, D. Samaras, and J. C. Joubert, X-ray analysis of the structural and dynamic properties $BaFe_{12}O_{19}$ hexagonal ferrite at room temperature, J. Solid State Chem. **56**, 171 (1985).

[61] G. Albanese, The dynamics of iron in pseudotetrahedral (bipyramidal) site of $BaFe_{12}O_{19}$ and $SrFe_{12}O_{19}$ hexagonal ferrites, Hyperfine Interact. **70**, 1087 (1992).

[62] M. A. P. Buzinaro, M. A. Macêdo, B. F. O. Costa, and N. S. Ferreira, Disorder of $Fe^{(2)}O_5$ bipyramids and spin-phonon coupling in $SrFe_{12}O_{19}$ nanoparticles, Ceram. Int. **45**, 13571 (2019).

[63] S. P. Marshall and J. B. Sokoloff, Phonon spectrum for barium ferrite, Phys. Rev. B **44**, 619 (1991).

[64] O. P. Aleshko-Ozhevskii, M. K. Faek, and I. I. Yamzin, A neutron diffraction study of the structure of magnetoplumbite, Sov. Phys. Crystallogr. **14**, 447 (1969).

[65] A. S. Mikheykin, E. S. Zhukova, V. I. Torgashev, A. G. Razumnaya, Y. I. Yuzyuk, B. P. Gorshunov, A. S. Prokhorov, A. E. Sashin, A. A. Bush, and M. Dressel, Lattice anharmonicity and polar soft mode in ferrimagnetic M-type hexaferrite $BaFe_{12}O_{19}$ single crystal, Eur. Phys. J. B **87**, 232 (2014).

[66] R. Comes, M. Lambert, and A. Guinier, The chain structure of $BaTiO_3$ and $KNbO_3$, Solid State Commun. **6**, 715 (1968).

[67] B. Dorner and R. Comes, Phonons and structural phase transformations, in *Dynamics of Solids and Liquids by Neutron Scattering. Topics in Current Physics*, edited by S. W. Lovesey

and T. Springer, 3rd ed. (Springer-Verlag, Berlin, Heidelberg, 1977), Vol. 3, pp. 127–192.

[68] N. A. Hill, Why are there so few magnetic ferroelectrics? J. Phys. Chem. B **104**, 6694 (2000).

[69] C. M. Fang, F. Kools, R. Metselaar, G. de With, and R. A. de Groot, Magnetic and electronic properties of strontium hexaferrite $SrFe_{12}O_{19}$ from first-principles calculations, J. Phys.: Condens. Matter **15**, 6229 (2003).

[70] A. K. Singh, D. Pandey, and O. Zaharko, Powder neutron diffraction study of phase transitions in and a phase diagram of $(1-x)[Pb(Mg_{1/3}Nb_{2/3})O_3] - xPbTiO_3$, Phys. Rev. B **74**, 024101 (2006).

[71] B. E. Vugmeister and M. D. Glinchuk, Dipole glass and ferroelectricity in random-site electric dipole systems, Rev. Mod. Phys. **62**, 993 (1990).

[72] U. T. Hochli, K. Knorr, and A. Loidl, Orientational glasses, Adv. Phys. **39**, 405 (1990).

[73] L. E. Cross, Ferroelectrics relaxor ferroelectrics: An overview, Ferroelectrics **151**, 305 (1994).

[74] R. A. Cowley, S. N. Gvasaliya, S. G. Lushnikov, B. Roessli, and G. M. Rotaru, Relaxing with relaxors: A review of relaxor ferroelectrics, Adv. Phys. **60**, 229 (2011).

[75] J. A. Mydosh, *Spin Glasses: An Experimental Introduction* (Taylor & Francis, London, 1993).

[76] K. Kumar, Discovery of new low temperature phase transitions in barium hexaferrite, Ph.D. thesis, Indian Institute of Technology, Banaras Hindu University, Varanasi, India, 2021.

[77] K. Kumar, A. Senyshyn, and D. Pandey, Evidence for emergent kagome spin configuration with concomitant transverse and longitudinal spin-glass freezing in the chemically ordered M-type hexaferrite $BaFe_{12}O_{19}$, arXiv:2111.15610.

[78] K. Kumar, S. K. Mishra, I. Baev, M. Martints, and D. Pandey, Evidence for the coexistence of spin-glass and ferrimagnetic phases in $BaFe_{12}O_{19}$ due to basal plane freezing, Chem. Commun. **56**, 14897 (2020).

[79] J. Mattsson, T. Jonson, P. Nordblad, H. A. Katori, and A. Ito, No phase transition in a magnetic field in the Ising spin glass $Fe_{0.5}Mn_{0.5}TiO_3$, Phys. Rev. Lett. **74**, 4305 (1995).

[80] S. E. Rowley, M. Hadjimichael, M. N. Ali, Y. C. Durmaz, J. C. Lashley, R. J. Cava, and J. F. Scott, Quantum criticality in a uniaxial organic ferroelectric, J. Phys.: Condens. Matter **27**, 395901 (2015).

[81] T. Kimura, S. Kawamoto, I. Yamada, M. Azuma, M. Takano, and Y. Tokura, Magnetocapacitance effect in multiferroic $BiMnO_3$, Phys. Rev. B **67**, 180401(R) (2003).

[82] T. D. Sparks, M. C. Kemei, P. T. Barton, R. Seshadri, E. D. Mun, and V. S. Zapf, Magnetocapacitance as a sensitive probe of magnetostructural changes in $NiCr_2O_4$, Phys. Rev. B **89**, 024405 (2014).

[83] G. Catalan, Magnetocapacitance without magnetoelectric coupling, Appl. Phys. Lett. **88**, 102902 (2006).

[84] R. Zhao *et al.*, Emergent multiferroism with magnetodielectric coupling in $EuTiO_3$ created by a negative pressure control of strong spin-phonon coupling, Nat. Commun. **13**, 2364 (2022).

[85] R. Tackett, G. Lawes, B. C. Melot, M. Grossman, E. S. Toberer, and R. Seshadri, Magnetodielectric coupling in Mn_3O_4, Phys. Rev. B **76**, 024409 (2007).